Chapter 5

Characterisation and application of tetrasubstituted N4Py iron complexes

5.1 Introduction

Several tetrasubstituted N4Py derivatives have been described in earlier chapters.[1] The synthesis of such pentadentate ligands was centred on the construction of a tetrafunctionalised N4Py derivative that would facilitate the covalent attachment of four peptide chains (Chapter 3). During the development of a synthetic pathway to this type of template, some N4Py derivatives were prepared enabling the spectroscopic features and the oxidation behaviour of their iron complexes to be examined. These experimental results will be presented and discussed in this chapter. Furthermore, the peroxidase activity of a N4PyFe-peptide complex will be described, as well as the stability of the sulphur linker that has been used to couple the peptides to the ligand.

5.2 Iron(II) complexes of tetrasubstituted N4Py ligands

The iron(II) complex **2a** of N4Py (**1a**) has previously been fully characterised and has shown to be a good functional mimic of the non-haem glycopeptide iron bleomycin (Fe–BLM).[2] A catalytic cycle was proposed for N4PyFe (summarised in Chapter 2),[2] which could also be applicable to Fe–BLM.

Several structural variations on **2a** have been carried out to ascertain the correlation between the composition of the iron(II) complex and its oxidation behaviour.[2b] These changes involved altering the oxidation state of the metal ion, the nature of axial ligand, and the N4Py ligand itself. Various mono- and disubstituted derivatives of **1a** and their iron complexes have been prepared and characterised as low-spin iron(II) complexes.[2] The complex **2a** will be referred to here only as a reference for the newly developed tetrasubstituted N4Py complexes **2b–f**.[2,3]

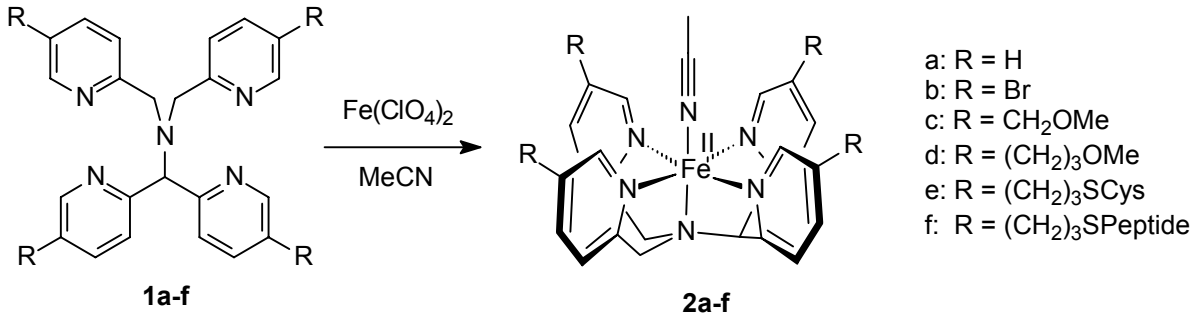

Scheme 5.1. The iron(II) complexes of N4Py (**1a**) and tetrasubstituted N4Py derivatives **1b–f** (peptide=Ac–CGLHELLKG–NH_2, coupled via the cysteine residue).[4]

Upon the addition of iron(II) perchlorate to the pentadentate ligands **1a–f** in acetonitrile the iron complexes **2a–f** were obtained (Scheme 5.1). The synthesis and characterisation of these tetrasubstituted N4Py derivatives **1b–f** have been described in earlier chapters. The corresponding iron complexes have not yet been discussed with the exception of **2e** and **2f**, which were described in Chapter 3.[5]

The ^{1}H NMR spectra of **2b–d** in CD_3CN revealed signals in the diamagnetic range of 0–10 ppm, which is distinctive for low-spin iron(II) complexes of N4Py ligands.[2] The UV-Vis absorption bands of **2b–f** (Table 5.2 p. 123, Figure 5.5 p. 122) also correlate well with those of the previously prepared iron(II) complexes of N4Py derivatives with maximum absorptions typically around 380 and 460 nm as expected.[2b,5] In addition, the electrospray ionisation mass analyses (ESI-MS) were in accordance with the postulated composition of the complexes **2b–d**.

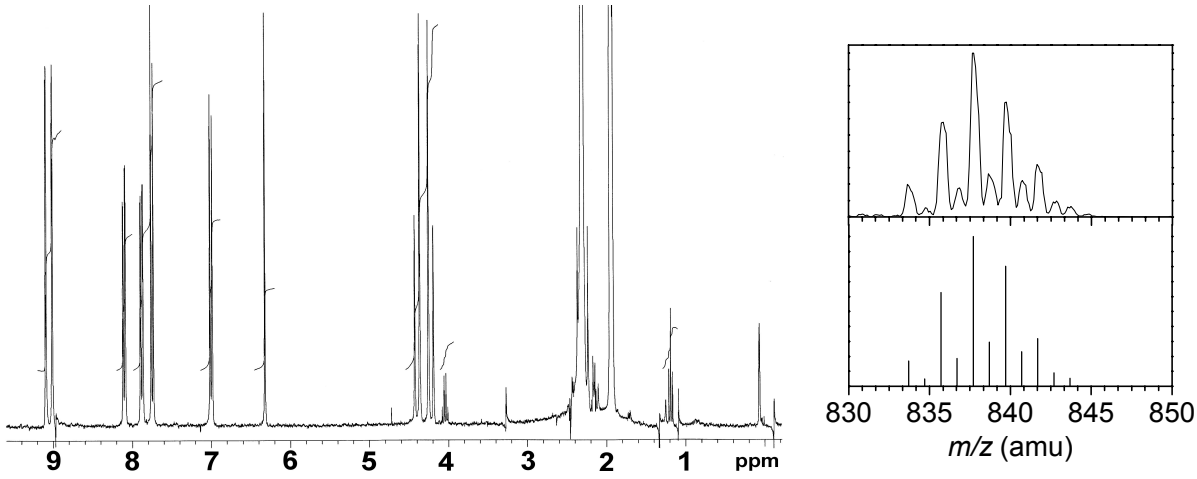

Figure 5.1. The ^{1}H NMR spectrum of **2b** in CD_3CN (left), and the observed and calculated isotope distribution patterns for [**2b**–$(ClO_4)^-$–(MeCN)]$^+$ (top and bottom right, respectively).

The solvent not only has an effect on the λ_{max} and the extinction coefficient (*vide infra*), but also on the stability of the iron(II) complexes of N4Py and its derivatives. In solvents such as acetone, methanol, or water the stability is limited to approximately one day, presumably due to the exchange of the axial ligand.[2b] Therefore, it is not surprising that these complexes are most stable in acetonitrile, for at least several weeks, as verified by UV-Vis spectroscopy.

The characteristic UV-Vis absorption bands for $[(N4Py4Br)Fe(MeCN)](ClO_4)_2$ (**2b**) in methanol were found to be extremely temperature-dependent. The individual absorption bands for **2b** around 380 and 460 nm could not be detected at 20°C, although these bands became more distinct as the temperature was lowered, which was accompanied by an increase in absorption (Figure 5.2). The extinction coefficient of **2b** at –10°C, however, is still significantly lower than that observed for **2a** under similar conditions (**2a**: λ_{max} 453 nm, ε 42 x 10^2 $M^{-1}cm^{-1}$; **2b**: λ_{max} 455 nm, ε 26 x 10^2 $M^{-1}cm^{-1}$).

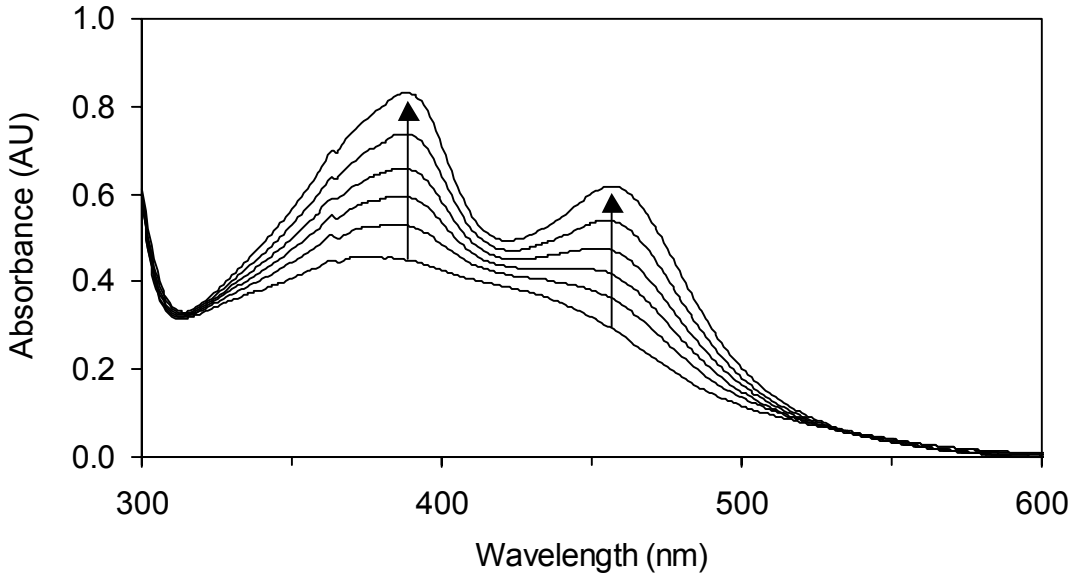

Figure 5.2. UV-Vis spectra of **2b**: increase in absorption in methanol as the temperature is lowered from 20°C to 5, 0, –5, –10, and –15°C, respectively.

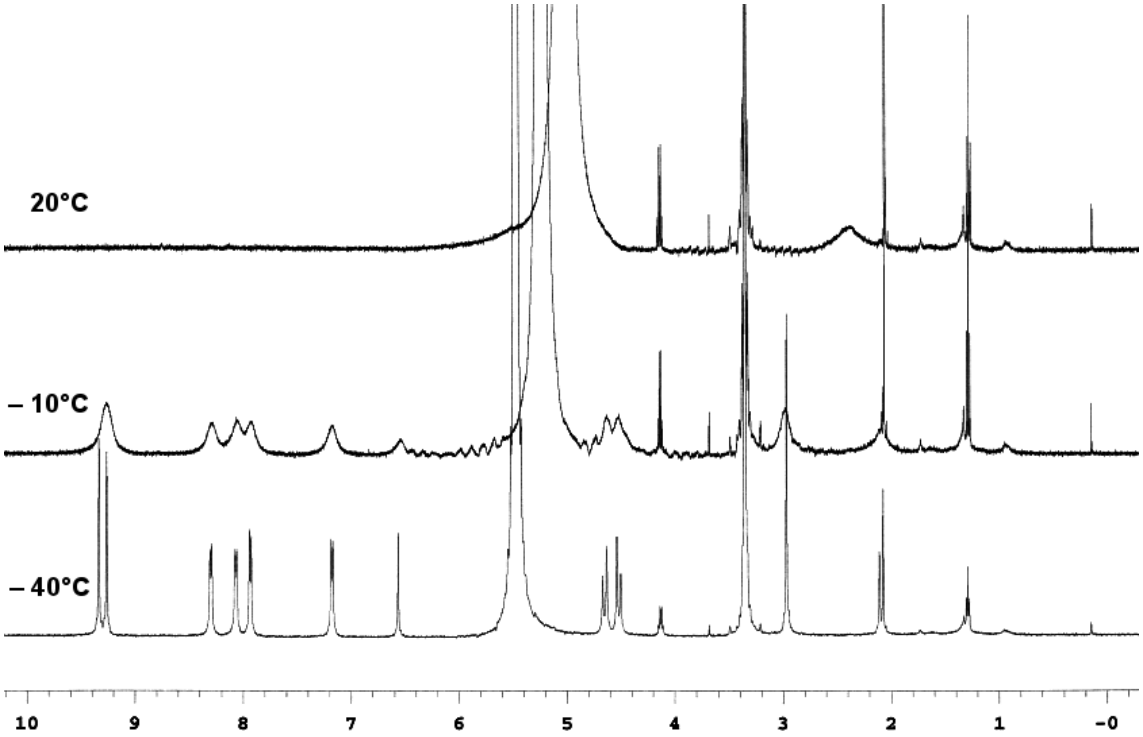

Figure 5.3. Temperature-dependent ^1H NMR spectra of **2b** in CD_3OD.

A plausible explanation for this temperature-dependent UV-Vis absorption of **2b** in methanol might be the initial formation of a high-spin $Fe^{III}OMe$ complex at room temperature. This species has previously also been described for **2a**,[2b] although it is not as readily formed as that of **2b**. As the temperature is then lowered, this species becomes a low-spin iron(II) complex. The spin transition was confirmed by temperature-dependent ^1H NMR analysis (Figure 5.3), which revealed a paramagnetic spectrum with very broad signals in the range of 0 to 100 ppm at 10°C and higher temperatures. At –10°C a diamagnetic spectrum was observed with well defined, although broadened signals from 0 to 10 ppm. The exact composition of this low-spin species and the process involved still need to be ascertained.

Crystals of the iron(II) complexes **2b** and **2c** suitable for X-ray analysis were obtained by the slow diffusion of ethyl acetate into their solutions in acetonitrile (Figure 5.4). Five co-ordination sites to the iron centre are occupied by the chelating ligand and a solvent derived acetonitrile molecule functions as an axial ligand. This mode of co-ordination to the metal ion is analogous to that observed for N4Py (**1a**).[3] As can be seen in Figure 5.4, the bromine atoms of **1b** and the side chains in **1c** are directed away from the iron centre in the complex. The same spatial arrangement can, therefore, also be predicted for other tetrasubstituted N4Py ligands with functional groups in the same positions as in **1b** and **1c**.

Although the iron-nitrogen bond lengths of **2b** and **2c** are comparable to those found for N4PyFe (**2a**), all of the bonds between the pyridine nitrogens and the iron centre ($Fe–N_{py}$) are shorter than was found for **2a** (Table 5.1). In contrast to **2a**, the bond lengths of the iron centre to the acetonitrile nitrogen ($Fe–N_{MeCN}$) in **2b** and **2c** are slightly elongated, whereas the bond lengths of the tertiary amine to the metal centre ($Fe–N_{amine}$) are comparable in all three complexes. Another difference is the distance of the iron centre above the mean plane that is constructed by the four equatorial pyridine nitrogen atoms ($Fe–N_{py–mean\ plane}$), which are identical in **2a** and **2b** but is shorter in **2c**. Electronic effects alone are, in our opinion, insufficient to explain these observations. Therefore, these minor differences in bond lengths in **2a**, **2b** and **2c** are most likely due to the differences in temperature during the X-ray analysis (See footnote in Table 5.1).

Table 5.1. Selected bond distances for **2b** and **2c**. The standard deviations are given in parentheses (**2a** is included for comparison).[a]

Bond (Å)		**2a**[3]	**2b**[6]	**2c**
$Fe–N_{amine}$	N1	1.961(3)	1.965(3)	1.958(3)
$Fe–N_{py}$	N2	1.976(3)	1.965(3)	1.957(3)
	N3	1.967(3)	1.956(3)	1.960(3)
	N4	1.968(3)	1.962(3)	1.960(3)
	N5	1.975(3)	1.970(3)	1.967(3)
$Fe–N_{MeCN}$	N6	1.915(3)	1.927(4)	1.928(3)
$Fe–N_{py–mean\ plane}$		0.2071(5)	0.207(1)	0.197(1)

a) X-ray diffraction of **2a** was performed at 130 K, **2b** at 90 K, and **2c** at 100 K.

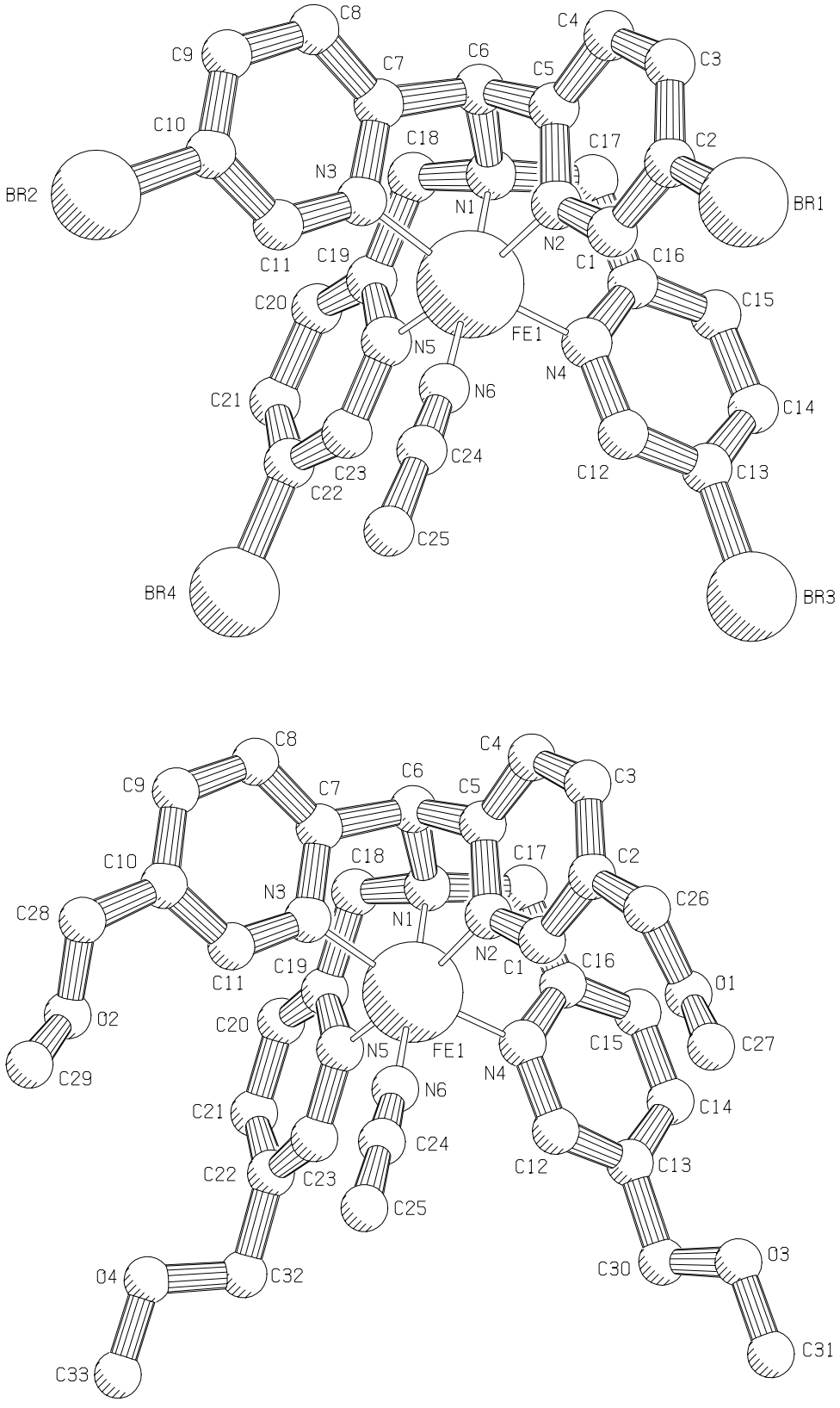

Figure 5.4. Pluto representation of **2b** (top) and **2c** (bottom). Hydrogen atoms and counterions are omitted for clarity.

5.3 Iron(III) hydroperoxo species

Upon the addition of excess hydrogen peroxide to **2a–f** the iron complexes are converted to the corresponding iron(III) hydroperoxo species **3a–f** (Scheme 5.2). The nature of this species was previously elucidated for N4PyFe (**2a**),[2] and the mechanism of its formation and further reaction is also considered to be applicable to other N4Py derivatives. In acetone the conversion to the hydroperoxide species ($Fe^{III}OOH$) is fast and complete, and can be monitored by UV-Vis spectroscopy (depicted in Figure 5.5 for **2a–d**). The complex **2e** can also be converted into its $Fe^{III}OOH$ species **3e**, although this was considerably less stable, was prepared as a model for peptide-bound N4PyFe complexes like **2f** to study the stability of the complex and its sulphur linker towards the applied oxidative conditions (*vide infra*).

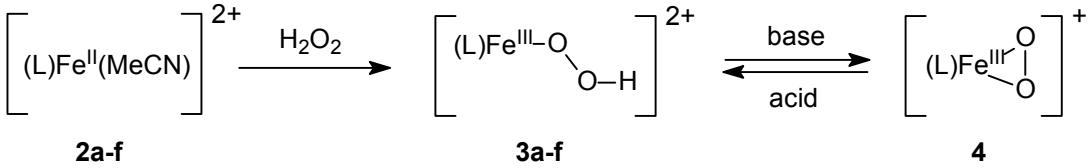

Scheme 5.2. Formation of the purple end-on $Fe^{III}OOH$ species **3a–f** from the corresponding iron(II) complexes **2a–f**, and the reversible conversion of **3a** to the blue $Fe^{III}O_2$ species **4**.

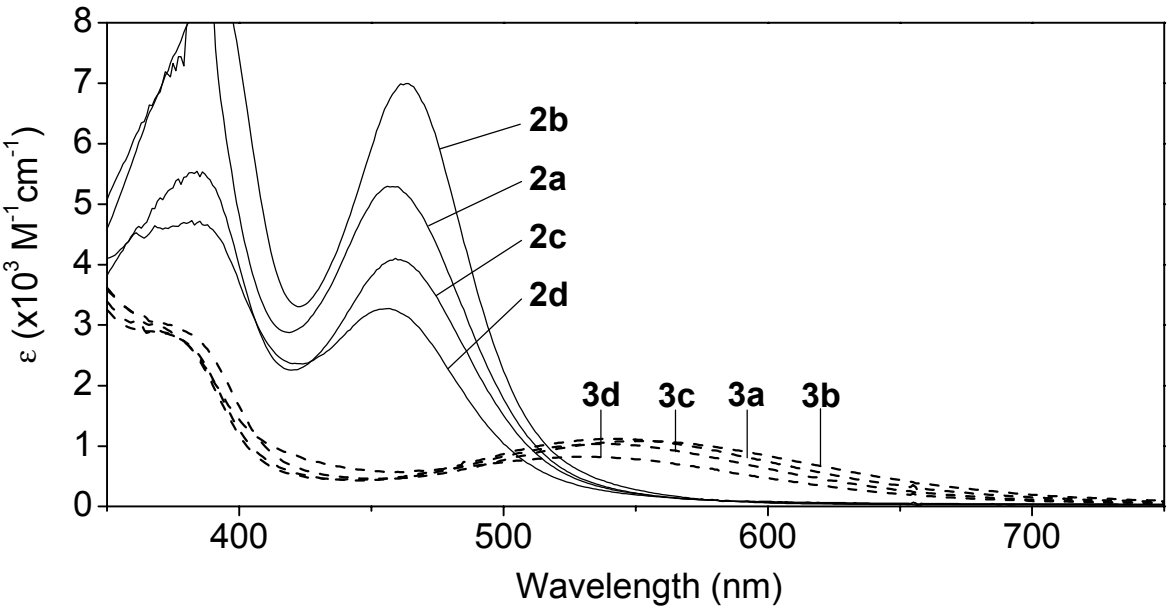

Figure 5.5. UV-Vis spectra of the iron(II) complexes **2a–d** (solid lines) and the corresponding $Fe^{III}OOH$ species **3a–d** (dashed lines) in acetone at 20°C.

The spectroscopic data for the iron(II) complexes **2a–d** and their iron(III) hydroperoxo species **3a–d** are summarised in Table 5.2 where acetone or acetonitrile was employed as the solvent. The purple intermediates **3b** and **3c** exhibit absorptions around 540 nm with extinction coefficients of 1000–1200 $M^{-1}cm^{-1}$, which are characteristic for low-spin end-on $Fe^{III}OOH$ species.[2,7] The lower extinction coefficients of **3d** and **3e** were attributed to the rapid decomposition of the intermediate, which is thought to occur during the conversion of the

iron(II) complex to the hydroperoxide species. The degradation of **3d** was also accompanied by a substantial amount of catalase activity, which involves the decomposition of hydrogen peroxide to dioxygen and water.

Similar to the complexes **2a–d**, the characteristics and the stability of the $Fe^{III}OOH$ intermediate was also found to be solvent-dependent. The general trend comprises of a small red shift for the iron(II) complexes on the exchange of acetonitrile as the solvent for acetone, which becomes more distinct for the corresponding $Fe^{III}OOH$ species. In addition, the complexes **2a–d** generally exhibit a higher extinction coefficient in acetonitrile, in contrast to their corresponding $Fe^{III}OOH$ species **3a–d**. This is considered to be caused by the unfavourable exchange of the axial ligand in acetonitrile, which results in a slow and incomplete formation of the peroxide species **3a–d**, and consequently leads to a lower absorption intensity for these intermediates.[2]

Table 5.2. Spectroscopic data of the Fe^{II} and $Fe^{III}OOH$ complexes of N4Py and its derivatives in acetone at room temperature.[a]

		$[(L)Fe^{II}(MeCN)](ClO_4)_2$		$[(L)Fe^{III}OOH](ClO_4)_2$	
Entry	Ligand (L)	λ_{max} (nm)	ε (x 10^2 $M^{-1}cm^{-1}$)	λ_{max} (nm)	ε (x 10^2 $M^{-1}cm^{-1}$)
1	**1a**	457 (455)	53 (48)	539 (520)	11 (7.2)
2	**1b**	464 (460)	70 (88)	553 (544)	11 (8.9)
3	**1c**	461 (457)	41 (59)	538 (522)	10 (7.8)
4	**1d**	457 (454)	33 (46)	531 (517)	8.2 (6.4)
5	**1e**[b]	456 (n.d.)	37 (n.d.)	525 (n.d.)	3.4 (n.d.)

a) The results in parentheses refer to acetonitrile as solvent. n.d. = not determined.
b) At 0°C, $\lambda_{max,\mathbf{2e}}$ 457 nm, ε 26 x 10^2 $M^{-1}cm^{-1}$; $\lambda_{max,\mathbf{3e}}$ 531 nm, ε 3.7 x 10^2 $M^{-1}cm^{-1}$.

It is known that a more electron-withdrawing ligand will be a weaker σ bond donor and a stronger π acceptor.[7] Consequently, the electron density on the metal centre will be decreased, thus resulting in a higher redox potential of the corresponding complex.[2b,7] The decrease in the energy of the ligand-to-metal charge transfer band for the $Fe^{III}OOH$ species will be accompanied by an increase in the λ_{max}.[2b,7] Substituents at the 5-position of the pyridine rings in disubstituted N4Py ligands were previously found to have only a minor electronic effect on the metal ion.[2b] However, the redox potential of the tetrabromide N4PyFe derivative **2b** was found to be substantially higher than that of N4PyFe **2a** ($E_{½}$ = 1010 mV vs. SCE)[2] and a dibromo N4PyFe derivative[8] ($E_{½}$ = 1100 mV vs. SCE).[2b] The cyclic voltammetry measurements for **2b** displayed a reversible oxidation wave with a redox potential for the Fe^{II}/Fe^{III} couple of 1198 mV vs. SCE and an observed peak-to-peak separation of 105 mV (Figure 5.6). Forward and reverse differential pulse voltammetry at a scan rate of 10 mVs^{-1} confirmed this process to be reversible with a redox potential for the Fe^{II}/Fe^{III} couple of 1196 mV vs. SCE.

The general trend infers that the introduction of a greater number of electron-withdrawing groups into the N4Py ligand results in an increase in the redox potential of the corresponding

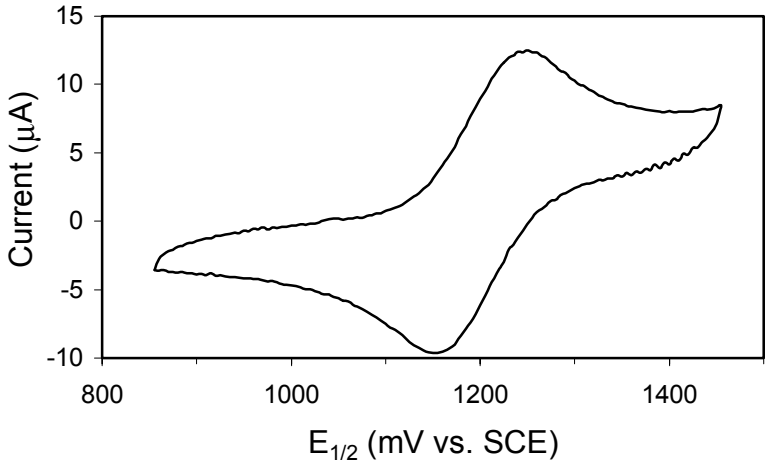

Figure 5.6. Cyclic voltammogram of **2b** in acetonitrile at 22°C (scan rate 100 mVs $^{-1}$).

iron(II) complex. This in turn gives rise to the observed relatively large red shift for the $Fe^{III}OOH$ species **3b** (Table 5.2, entries 1 and 2). The electronic effect of the methoxymethyl groups or the alkyl spacers in **3c** and **3d** influence the absorption maxima only to a minor extent. Unfortunately, as the redox potentials for **2c** and **2d** have not yet been determined, conclusive evidence cannot be provided for the relationship between the redox potential of N4PyFe complexes and the absorption maximum of their iron(III) hydroperoxo species.

The $Fe^{III}OOH$ species of **2e** could not be detected by a stepwise titration of the iron(II) complex with hydrogen peroxide in acetone at room temperature. However, when a single aliquot of excess hydrogen peroxide was added to **2e** the intermediate **3e** could be observed for a limited period. Its lifetime was significantly extended to approximately fifteen minutes by reducing the temperature of the solution to 0°C. The pH appeared to have only a minor effect on the extinction coefficient of **2e** (λ_{max} 452 nm, $\varepsilon_{pH\ 4}$ 35 x 10^2 $M^{-1}cm^{-1}$, $\varepsilon_{pH\ 7}$ 38 x 10^2 $M^{-1}cm^{-1}$, $\varepsilon_{pH\ 10}$ 33 x 10^2 $M^{-1}cm^{-1}$) at room temperature. The intermediate **3e** could not be detected even under these conditions. A fine light yellow solid was always observed in the cuvette subsequent to these UV-Vis experiments. Unfortunately, the identity of this material could not be established by mass analysis. Nevertheless, it was hypothesised that this residue could be the product from the oxidative degradation of the ligand. Similar observations were made when employing the dipeptide-bound N4PyFe complex described in Chapter 2.[9]

In an attempt to oxidise 1,2,4,5-tetramethoxybenzene (Scheme 5.5C, p. 130) by **2e** the oxidation reaction was monitored by ESI-MS at room temperature. It was verified that a rapid decomposition of the catalyst occurred in the absence of any detectable oxidation of the substrate (Figure 5.7). Although the intensities of the peaks cannot be quantified, it is clear that the disappearance of **2e** (*m/2z* 646.0 amu for $[M-2(ClO_4)^- - (MeCN)]^{2+}$) is accompanied by the formation of a new, related species, possibly from the oxidation of the sulphur atoms in ligand **1e**.

One suggestion for the assignment of the peak at 654.6 amu is the introduction of one oxygen atom in the doubly-charged species from **2e**. The mass of 670.4 amu could originate from the complex **2e** after the oxidation of three sulphur atoms to the corresponding sulphoxides. If so, it still remains a mystery as to why no further oxidation of the sulphur linkers was observed. The visual observations during the UV-Vis experiments, however, did confirm that the catalyst had decomposed under the employed oxidative conditions (*vide supra*). The

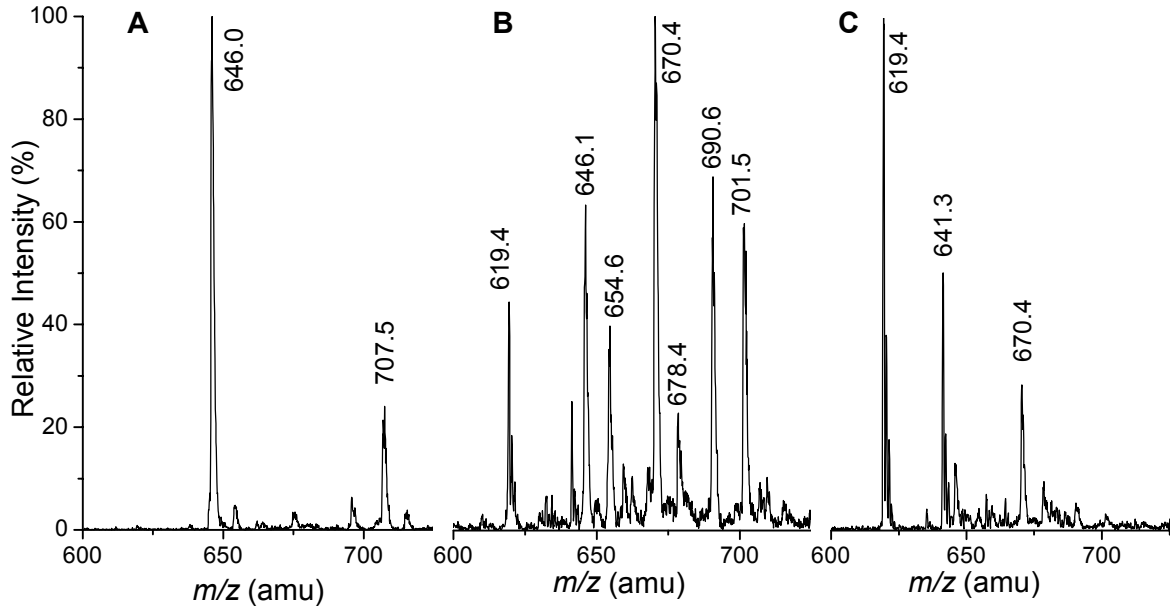

Figure 5.7. ESI-MS analysis for the oxidation of 1,2,4,5-tetramethoxybenzene by **2e** (*m/2z* 646.0 amu) at room temperature by hydrogen peroxide at t = 0 (A), t = 1 min (B), and t = 20 min (C).

masses at *m/z* 619.4 and 641.3 were assigned to singly-charged species, although their exact identity still remains unknown, as is the structure of the doubly-charged species at *m/z* 690.6 and 701.5. These observed masses, however, also cannot be assigned to the corresponding $Fe^{III}OOH$ intermediate.

The iron(III) hydroperoxo species **3a** (λ_{max} 548 nm, ε 12 x 10^2 $M^{-1}cm^{-1}$) can be deprotonated reversibly to the conjugate base **4** (λ_{max} 690 nm, ε 440 $M^{-1}cm^{-1}$) in methanol at –10°C (Scheme 5.2). UV-Vis, EPR, and resonance Raman spectroscopy as well as ESI-MS analysis established the nature of this high-spin $Fe^{III}-\eta^2-O_2$ species **4**.[10] It can be assumed that this interconversion will also be applicable to the iron(II) complexes of N4Py derivatives in general.

Although the purple intermediate **3b** can be generated readily in acetone and acetonitrile at 20°C, in methanol this conversion is by no means complete (λ_{max} 557 nm, ε 3.5 x 10^2 $M^{-1}cm^{-1}$). Surprisingly, no significant formation of **3b** was observed at –10°C in methanol. Instead a new small absorption at 509 nm was detected (Figure 5.8). Presumably, the axial methoxy ligand in the $Fe^{III}OMe$ species that is formed *in situ* is bound too strongly to the metal ion, and thus prevents a facile conversion to the purple intermediate **3b**. The addition of base resulted in the immediate disappearance of the absorption bands for the observed intermediate, but did not lead to the formation of a $Fe^{III}-\eta^2-O_2$ species as found for **3a**. This was surprising as it was assumed that the electron-withdrawing bromides in the $Fe^{III}OOH$ species **3b** would promote its deprotonation. However, if the $Fe^{III}OOH$ species is not formed due to the strongly bound methoxy ligand, then this would explain the absence of the corresponding blue species.

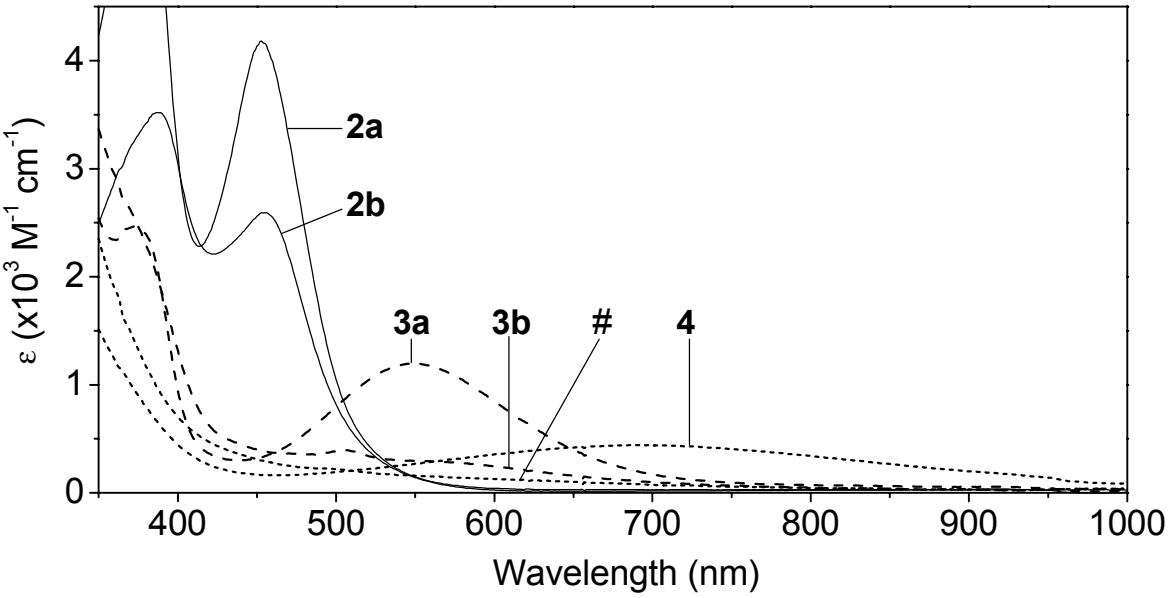

Figure 5.8. UV-Vis spectra of **2a** and **2b** in methanol at −10°C (thin solid lines), after the addition of 5 equiv H_2O_2 (dashed lines), and 5 equiv NH_4OH (dotted lines) (# = **3b** + 5 equiv NH_4OH).

5.4 Oxidation of organic substrates

As previously observed for **2a**, its $Fe^{III}OOH$ species is capable of oxidising a variety of organic substrates such as benzene, styrene, benzyl alcohol, cyclohexene and cyclohexane.[11] The proposed mechanism for the oxidation of alkanes was discussed and summarised in Chapter 2.[2b,11b]

$$\underset{\textbf{3a}}{[(N4Py)Fe^{III}O{-}OH]^{2+}} \xrightarrow[\text{cleavage}]{\text{homolytic}} [(N4Py)Fe^{IV}{=}O]^{2+} + {\bullet}OH$$

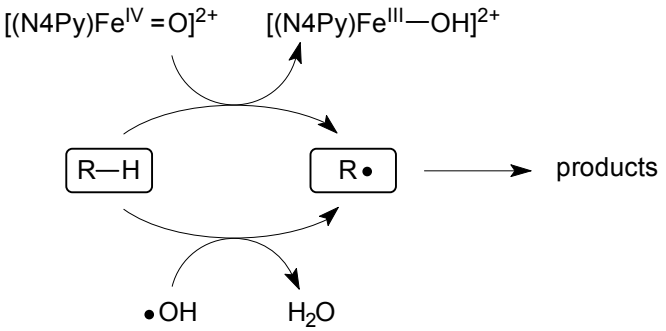

Scheme 5.3. Proposed mechanism for substrate (R−H) oxidation by **3a**.[2b]

The influence of the substituents in the ligands **1b–d** towards the oxidation behaviour of the corresponding iron(II) complexes **2b–d** was examined using the substrates cyclohexene (**5**) and cyclohexane (**9**) (Scheme 5.4). These substrates were selected due to their high turnover (expressed in TON, mol product per mol catalyst) in oxidation reactions catalysed by **2a** and thereby provided a suitable basis on which to assess the catalytic activity of **2b–d**.

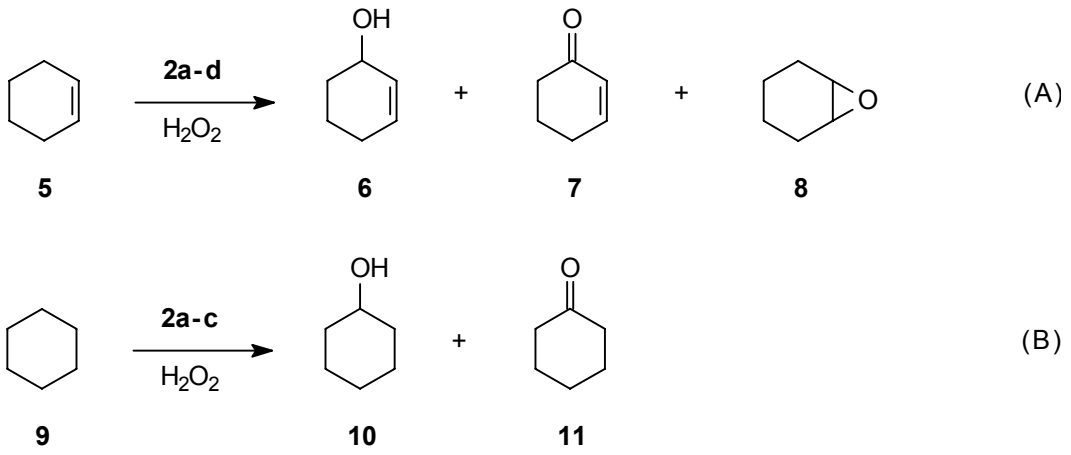

Scheme 5.4. The anticipated products for the oxidation of cyclohexene (A) and cyclohexane (B).

The catalytic oxidation reactions were carried out in acetone or acetonitrile at 20°C under a nitrogen atmosphere in the presence of an excess of substrate (substrate/H_2O_2/catalyst = 1000:100:1). The catalysts **2a–d** were used as a stock solution in acetonitrile. The oxidation was initiated by the addition of a single aliquot of hydrogen peroxide. Within the examined time-span a blank reaction by hydrogen peroxide could not be detected, even in the presence of an equal catalytic quantity of iron perchlorate. Therefore, the observed oxidation of the substrates was solely attributed to the catalytic activity of **2a–d**. The conversions of **5** and **9** over time employing acetone as the solvent are shown in Figure 5.9 and Figure 5.10, respectively. Table 5.3 summarises the TONs of the catalysts when subjected to a reaction time of one hour.

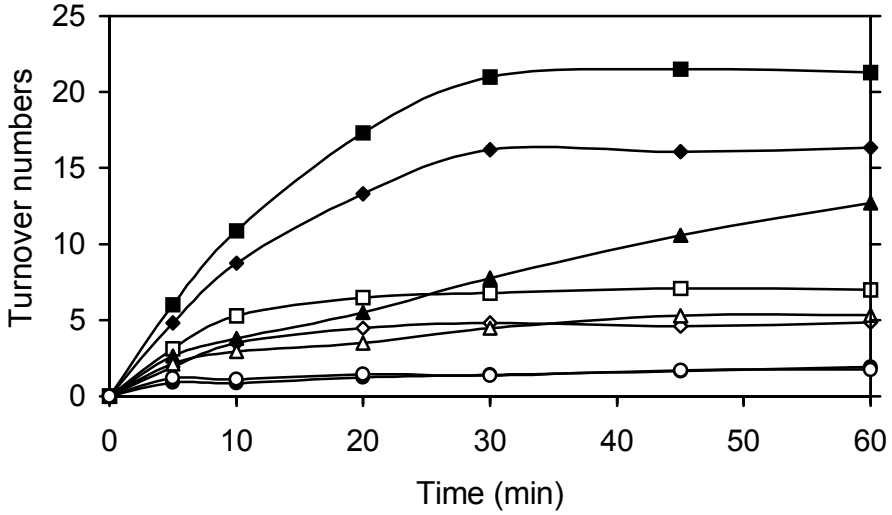

Figure 5.9. Catalytic oxidation of cyclohexene to cyclohexenol (solid) and cyclohexenone (open) by hydrogen peroxide in acetone at 20°C (**2a**: –■–,–□–; **2b**: –◆–,–◇–; **2c**: –▲–,–△– ; **2d**: –○–,–●–).

The iron(II) complex **2a** is clearly the most active catalyst of all the complexes **2a–d** for the oxidation of cyclohexene. The final TON of 21.3 for **2a** (Table 5.3, entry 1) was comparable to the previously reported TON of 23.1.[11b] Although the purple colour of the $Fe^{III}OOH$

intermediates **3a–c** disappeared after approximately 15 minutes, the oxidation reaction ceased after a further 15 minutes for **2a** and **2b**, as can be seen in Figure 5.9 and Figure 5.10. This observation was not attributed to a complete deactivation of the catalyst, as the addition of further hydrogen peroxide caused the reaction to recommence. The same was also applicable to **2b**, which, although less active than **2a**, displayed a similar oxidation behaviour over time.

Within the timeframe of one hour the reactivity of the catalyst **2c** towards cyclohexene was not only lower than that of **2a** or **2b**, it was also almost linear as opposed to the exponential curves as observed for **2a** and **2b**. In addition, the dissipation of the curves for **2c** in Figure 5.9 indicates an increased product selectivity over time. The catalyst **2d** seemed to be deactivated almost immediately and consequently did not yield more than two turnovers (Table 5.3). In all the above cases, the oxidation product cyclohexene oxide (**8**) was only formed in minute quantities, if at all.

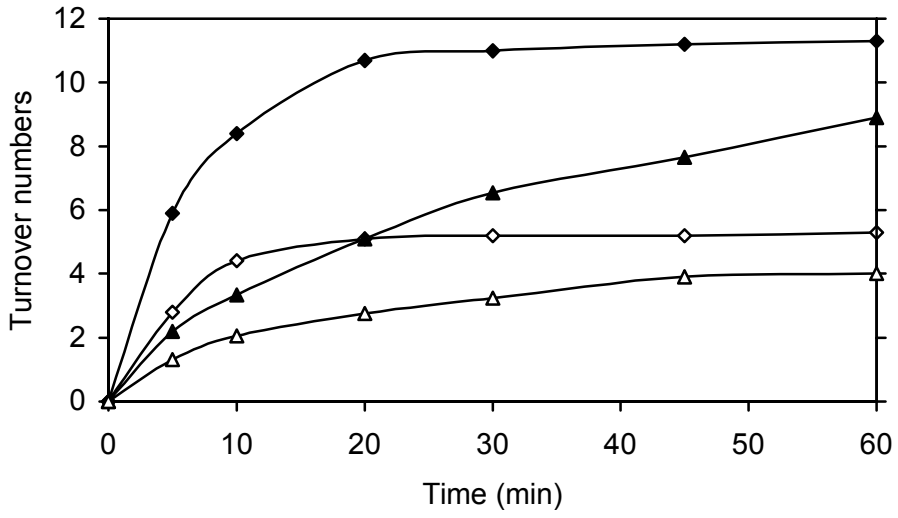

Figure 5.10. Catalytic oxidation of cyclohexane to cyclohexanol (solid) and cyclohexanone (open) by hydrogen peroxide in acetone at 20°C (**2b**: –◆–,–◇–; **2c**: –▲–,–△–).

In the oxidation of cyclohexane the behaviour of the catalysts **2b** and **2c** was comparable to that shown in Figure 5.9. As before, the iron(II) complex **2b** was found to be less reactive than **2a** (Table 5.3, entry 2) and the conversion ceased after approximately thirty minutes. In addition to this, the activity of **2c** proceeded beyond the allocated reaction time of one hour, which was accompanied by an increased selectivity over time. Due to the previously observed deactivation of the catalyst **2d**, this iron(II) complex was not examined for the oxidation of cyclohexane.

In order to determine the maximum number of turnovers for each catalyst, an excess of hydrogen peroxide was slowly administered to the reaction mixture over one hour. The results in Table 5.3 (in brackets) not only illustrated that a higher turnover can be obtained, but also that the selectivity of the reaction is inverted when cyclohexene is employed as the substrate. This selectivity is best expressed as the ratio of alcohol over ketone product (A/K). The ratios in Table 5.4 indicate that this selectivity is virtually unaffected using the substrate cyclohexane, which suggests that the mechanism involved is also unaffected. In general, an A/K ratio of one

Table 5.3. Turnover numbers of the iron(II) complexes of N4Py and its derivatives for the catalytic oxidation reactions in acetone after one hour at room temperature.[a]

Entry	Substrates	Products	**2a**	**2b**[b]	**2c**	**2d**
1	cyclohexene	**6**	21 (24)	16 (17)	13 (14)	2 (2)
		7	7 (5)	5 (27)	5 (31)	2 (4)
		8	– (13)	0.1 (3)	2 (8)	1 (2)
2	cyclohexane	**10**	17[c]	11 (16)	9 (16)	n.d.
		11	7[c]	5 (9)	4 (6)	n.d.

a) Results in parentheses refer to a slow addition of 2000 equiv H_2O_2 over one hour.
b) TONs in acetonitrile as the solvent: **6**: 8, **7**: 5, **8**: –.
(Compared to N4PyFe:[c] **6**: 28, **7**: 7, **8**: 1)
c) Taken from the Ph. D. thesis of Gerard Roelfes.[2,11b]

will be obtained if free radical intermediates are involved in the reaction,[12] which can react, for instance, with dioxygen to propagate a radical chain auto-oxidation process. This ratio is only observed for the oxidation of cyclohexene by **2d**. In light of the calculated A/K ratio and the catalase activity during the UV-Vis experiments (*vide supra*), the decomposition of **2d** is attributed to the formation of free radicals during the oxidation reaction.

Table 5.4. The ratios of alcohol (A) over ketone (K) product formation in acetone at 20°C.[a]

Entry	Catalyst	A/K (cyclohexene)	A/K (cyclohexane)
1	**2a**	3.0 (0.4)	2.6 (n.d.)[b]
2	**2b**	3.4 (0.6)	2.1 (1.7)
3	**2c**	2.4 (0.5)	2.2 (2.6)
4	**2d**	1.1 (0.5)	n.d.

a) Results in parentheses refer to a slow addition of 2000 equiv H_2O_2 over 1 h.
b) Taken from the Ph. D. thesis by Gerard Roelfes.[2]

The $Fe^{III}OOH$ intermediate in the presence of hydrogen peroxide is capable of oxidising alcohols like cyclohexanol to the corresponding ketone.[11b] However, the observed A/K < 1 for cyclohexene upon the slow addition of excess hydrogen peroxide is not due to the *in situ* oxidation of the alcohol to the ketone, as the A/K ratios were found to be relatively constant for **2b** and **2c** during and after the addition of hydrogen peroxide. It was previously established that slow addition of 100 equivalents of hydrogen peroxide leads to an increase in the A/K ratio.[11b] Presumably, the addition of 2000 instead of 100 equivalents of hydrogen peroxide with respect to the catalyst has affected the rate-determining step of the reaction, or altered the mechanism. However, at the present time no conclusive evidence can be provided to either support or disprove this conjecture. A full kinetic study will have to be undertaken to provide such

evidence. The higher hydrogen peroxide concentration can also give rise to more decomposition by catalase. The produced dioxygen in turn can react with free radicals present to propagate the radical chain process,[12] but this would result in A/K ratios of one as opposed to the observed values of less than one.

5.5 Assays for screening peroxidase activity

Peroxidases catalyse the oxidation of a wide range of substrates using hydrogen peroxide as the terminal oxidant.[13] Their huge structures, however, make it difficult to study or determine the factors that govern their function and behaviour. Therefore, microperoxidases (right) are commonly used as models for these haemoproteins.[14,15,16] These small haem-peptide fragments can be obtained by the proteolytic digestion of cytochromes *c*, and contain a small peptide fragment that is covalently linked to the haem via two cysteine residues.

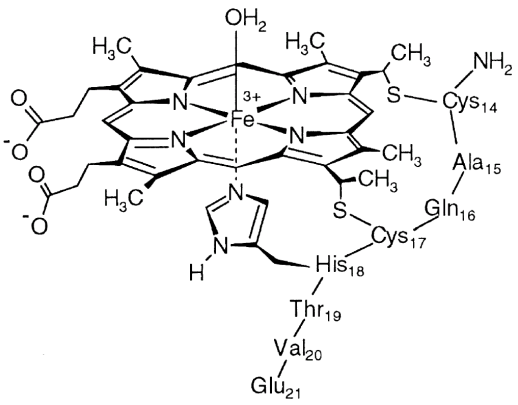

Substrates that are used to investigate the peroxidase activity of newly developed peroxidases or their mimics are usually probes that enable their conversion to be monitored by UV-Vis spectroscopy.[17] A typical reaction to test for peroxidase activity involves the oxidation of *o*-methoxyphenol (**12**) to compound **13**,[18] which is sometimes referred to as tetraguaiacol (Scheme 5.5A).[14b,19,20] When subjected to the oxidising conditions the substrate 2,2'-azinobis-(3-ethyl-benzothiazoline-6-sulphonic acid) (ABTS, Scheme 5.5B) is converted into a radical cation (*vide infra*).[15,21] Even though these probes can be readily applied as assays for peroxidase activity, they do not enable the selectivity of the catalyst to be monitored. The probe tetramethoxybenzene[22] (**14**) creates an opportunity to determine the product selectivity of the

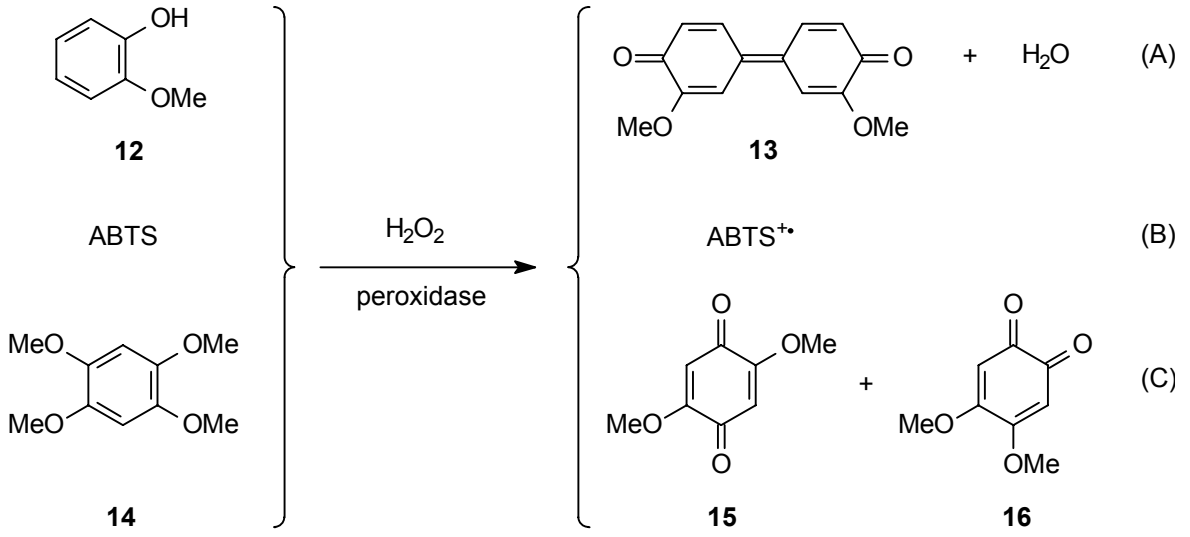

Scheme 5.5. Assays for screening peroxidase activity.

peroxidation reaction that is catalysed by the (artificial) enzyme or mimic (Scheme 5.5C).[23] A drawback for this assay, however, is that it necessitates the need for a standardised HPLC method to quantify the product distribution.

5.6 Oxidation of ABTS by non-haem catalysts

The peroxidase activity and the pH-dependency of N4PyFe (**2a**) and the peptide complex **2f** were determined by monitoring spectrophotometrically the formation of the emerald green $ABTS^{+\bullet}$ radical cation over time at 660 nm (ε 1.47 x 10^4 $M^{-1}cm^{-1}$).[16b] This probe had also been used to establish the peroxidase activity of the dipeptide-bound N4PyFe catalyst presented in Chapter 2.[24]

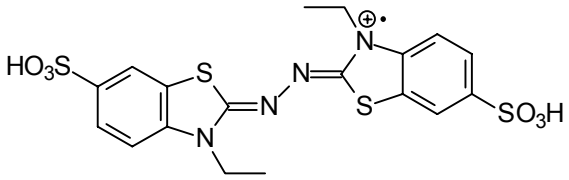

Figure 5.11. The ABTS radical cation.

It has been established that the rate limiting step for microperoxidases and other peroxidase enzymes is the formation of the reactive intermediate.[14a,15b,16,19d] This process obeys pseudo-first-order kinetics at low concentrations. Under the same conditions these kinetics could also apply to the peroxidation of ABTS using the non-haem catalysts **2a** or **2f**. However, a full kinetic study has not yet been undertaken to establish the kinetics for this reaction. The following discussion is purely speculative with regards to the observed formation of $ABTS^{+\bullet}$ and the factors that could influence the peroxidation reaction.

By employing an ABTS/H_2O_2/catalyst ratio of 500:1000:1 the concentration of the substrate and the oxidant can be considered to have little or no effect on the rate of the reaction. The reactions were initiated by the addition of hydrogen peroxide to a thermostatically controlled and buffered (AcOH/NaOAc) solution of the substrate and the catalyst. The previously established optimal pH range of 3.0 to 4.5 was employed to study the catalytic activity of **2a** during the peroxidation of ABTS.[24]

The highest initial rate for the peroxidation by **2a** was observed at pH 3.5 (Figure 5.12A). The observed curvatures in the formation of $ABTS^{+\bullet}$ (Figure 5.12) were attributed to the deactivation of the catalyst. Similar oxidative degradation of the catalyst is also common for microperoxidases and haem oxygenases.[14a,15b,16,25] The catalyst is completely deactivated within approximately 100–400 seconds, depending on the applied pH. The continued formation of $ABTS^{+\bullet}$ originates from the non-catalysed peroxidation of ABTS by hydrogen peroxide. This is the main disadvantage of using ABTS as a probe for peroxidation activity. As a result, the experimental data for the peroxidation of ABTS catalysed by iron perchlorate, N4PyFe (**2a**), and the peptide-bound complex **2f** has to be corrected for this background reaction, which accentuates the deactivation of the catalyst over time (Figure 5.12B).

When compared to N4PyFe, the N4PyFe-peptide complex **2f** displayed a substantially lower activity for the peroxidation of ABTS under identical conditions (Figure 5.12B). This result

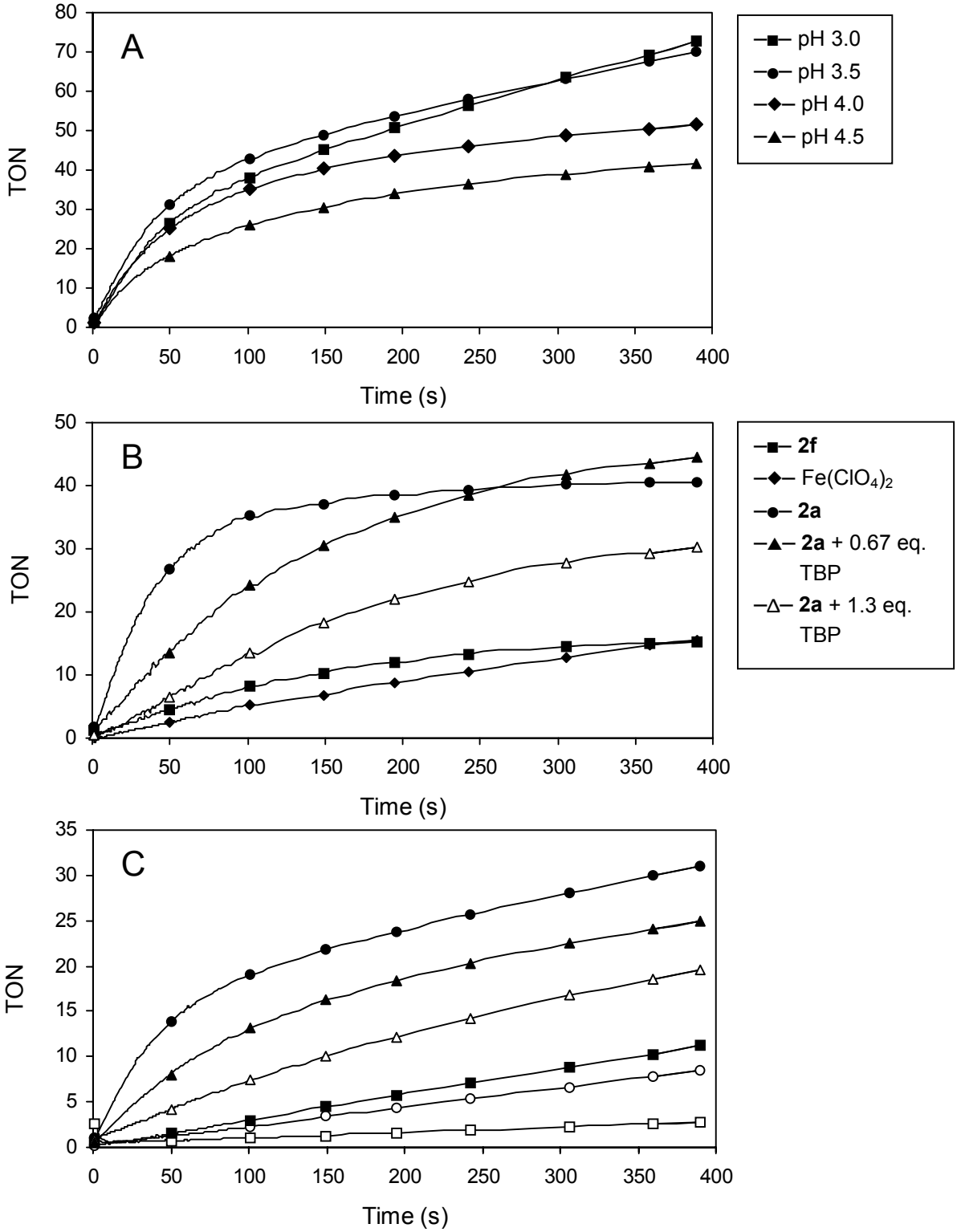

Figure 5.12. Formation of the $ABTS^{+\bullet}$ radical cation over time at 20°C, expressed in turnover numbers (TON). (A) pH-dependency of **2a**; (B) background corrected oxidation of ABTS by **2a**, **2f**, and iron(II) perchlorate at pH 3.5, and by **2a** in the presence of the radical scavenger 2,4,6-tri-*tert*-butylphenol (TBP); (C) effect of TEMPO on the catalytic activity of **2a** at pH 3.5 (–○– background reaction by H_2O_2; –●– H_2O_2 and **2a**; –□– TEMPO; –■– TEMPO and H_2O_2; –▲– H_2O_2 and **2a** in the presence of 0.3 equiv TEMPO with respect to H_2O_2; –Δ– H_2O_2 and **2a** in the presence of 1 equiv TEMPO with respect to H_2O_2).

is attributed to the steric interactions between the peptide chains of the catalyst and the ABTS substrate. However, these peptides appear to prolong the lifetime of the catalyst from approximately 150 to almost 400 seconds. It was already established that a reduction in temperature extends the lifetime of the $Fe^{III}OOH$ intermediate **3f** (*vide supra*). Therefore, by lowering the temperature and changing the solvent to acetone for example, the oxidative decomposition of the complex by the hydroxyl radicals might be reduced. The use of another, smaller substrate molecule like 1,2,4,5-tetramethoxybenzene (**14**) might also improve the catalytic turnover by reducing the steric interactions.

The turnover towards the end of the reaction period is also far too low to support the reduced reaction rate of $ABTS^{+\bullet}$ formation due to a complete consumption of hydrogen peroxide. This observation was further validated upon the addition of more hydrogen peroxide, which did not appear to affect the reaction. The addition of a new batch of catalyst **2a**, however, was able to induce a small and brief increase in the reaction rate. An initial increase in the catalyst loading also led to an enhanced reaction rate.

It has been suggested that hydroxyl radicals are involved in the catalytic oxidation of alkanes by N4PyFe (**2a**).[2b] The oxidation of ABTS to $ABTS^{+\bullet}$ can also be accomplished efficiently by hydroxyl radicals only.[26] Furthermore, these strongly oxidising species, as well as hydrogen peroxide itself, could be the source of the catalyst's degradation.

If the rate-determining step of the peroxidation by **2a** involves the formation of the $Fe^{III}OOH$ intermediate, then the addition of a hydroxyl radical scavenger should not have any effect on the initial reaction rate but only on the lifetime of the catalyst. However, the addition of tri-*tert*-butylphenol, an efficient radical scavenger,[16b] not only gave rise to an increased lifetime of the catalyst, but also to a reduction in the reaction rate (Figure 5.12B). These observations imply that the rate determining step does not in fact involve the formation of the transient $Fe^{III}OOH$ intermediate, but rather the reaction of the reactive species with the substrate ABTS. Trapping these hydroxyl radicals and/or the proposed one-electron oxidation species $[(N4Py)Fe^{IV}(O)]^{2+}$ (Scheme 5.3) with the scavenger will consequently result in the observed drop in the reaction rate. In addition, these findings strongly support the suggestion that hydroxyl radicals are involved in the catalytic cycle of **2a**.[2b,11b]

A drop in the rate of $ABTS^{+\bullet}$ formation was also observed when the free radical 2,2,6,6-tetramethylpiperidin-1-oxyl (**17**, TEMPO) was used for the reaction catalysed by **2a** (Figure 5.12C). The addition of 2,2,6,6-tetramethylpiperidine (TEMP) had a similar, but less pronounced, negative effect on the reaction rate (not shown). However, the use of either of these reagents did not lead to an extended lifetime for the catalyst. The effect of TEMPO and TEMP was dependent upon the amount that was added to the reaction mixture. Although ABTS has also been applied as a scavenger of free radicals like hydroxyl and bromine radicals, as well as ferryl porphyrins,[27] TEMPO itself was not able to oxidise efficiently ABTS to the $ABTS^{+\bullet}$ radical cation (Figure 5.12C). In fact, the reaction of TEMPO with ABTS was substantially slower than that observed for hydrogen peroxide, even in the presence of **2a** (not shown). The combination of hydrogen peroxide and TEMPO resulted only in a minor increase in the rate of the background reaction (Figure 5.12C).

From these observations it can be concluded that TEMPO reacts with the $Fe^{III}OOH$ intermediate and interferes with the homolytic O–O bond dissociation. Consequently, the formation of the hydroxyl radicals and the one-electron $[(N4Py)Fe^{IV}(O)]^{2+}$ species is hampered

(Scheme 5.3). The mechanism involved could be related to the suggested mechanism for the oxidation of alcohols using TEMPO.[28] The oxoammonium salt **18**, formed by a disproportionation of TEMPO (**17**), can react with the $Fe^{III}OOH$ species **3a**, as shown in Scheme 5.6. The equilibrium between **18** and **20** subsequently can result in the slow release of **3a**, and therefore in a slower formation of the hydroxyl radicals and $[(N4Py)Fe^{IV}(O)]^{2+}$, which leads to the reduced rate of the ABTS peroxidation and the catalyst degradation. Although highly speculative, this conjecture can account for the observations shown in Figure 5.12.

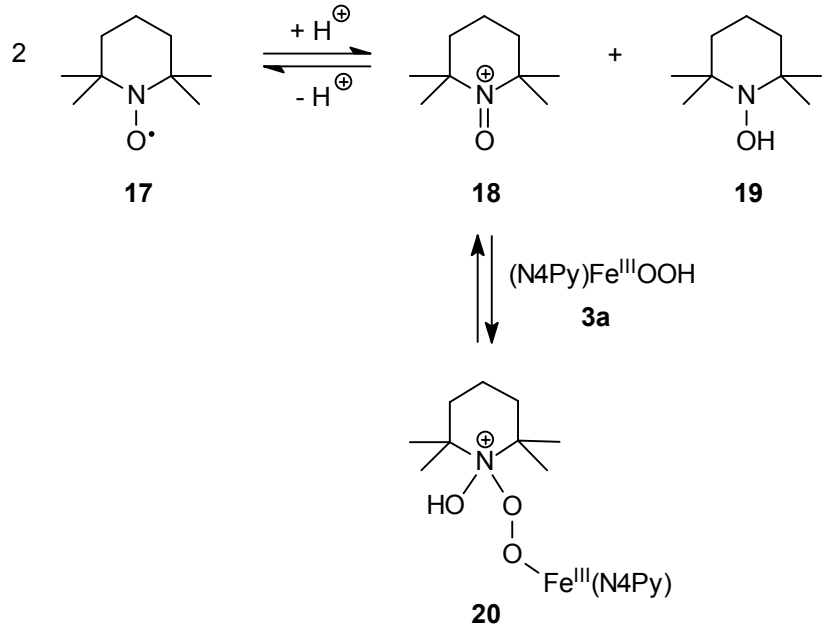

Scheme 5.6. Proposed mechanism for trapping the $Fe^{III}OOH$ intermediate by TEMPO.

UV-Vis experiments in acetone at room temperature independently established that the addition of TEMPO and TEMP to the purple $Fe^{III}OOH$ intermediate resulted in the immediate disappearance of its absorption band. If TEMPO was added before the addition of hydrogen peroxide, the formation of $Fe^{III}OOH$ was substantially slower and incomplete. The interaction between TEMP and $Fe^{III}OOH$ might be due to a simple acid/base reaction. Under these conditions the anticipated blue $[(N4Py)Fe^{III}-\eta^2-(OO)]^+$ species **4** was indeed detected by means of a very low and broad absorption band (λ_{max} 705 nm). The low stability was attributed to the employed solvent and temperature.

5.7 Discussion and conclusions

The introduction of four substituents at the 5-position of the pyridine rings in the N4Py ligand was found to influence the characteristic absorption maxima and the extinction coefficients of the corresponding iron(II) complexes only to minor extent. These results, therefore, infer that the proposed mechanism for the $Fe^{III}OOH$ formation from N4PyFe (**2a**) also applies to a broader range of N4Py derivatives. However, the exact nature of the substituent determines the stability and reactivity of the $Fe^{III}OOH$ intermediate, either by altering the redox potential of the iron complex, as in the case of **2b**, or by (presumably) the intramolecular oxidative degradation of the catalyst, as observed for **2d**.

The tetrasubstituted N4PyFe derivatives **2b** and **2c** proved to be active catalysts for the oxidation of cyclohexene and cyclohexane. Although reduced, the longer lasting reactivity of **2c** indicates that by tuning the substituents on the N4Py ligand the lifetime of the catalyst can also be prolonged.

The peroxidase activity of N4PyFe (**2a**) was found to be strongly pH-dependent, which might be due to a pH-controlled destruction of the catalyst, as a higher activity leads to a more rapid degradation of the catalyst. The synthesised N4PyFe-peptide complex **2f** also displayed peroxidase activity as demonstrated by the oxidation of chromogen ABTS. Although the observed activity is substantially lower than that of **2a**, a significantly higher activity compared to the background reaction by hydrogen peroxide was observed. Furthermore, the lifetime of catalyst **2f** was longer than that of **2a**. Mass spectrometry analysis during the oxidation of 1,2,4,5-tetramethoxybenzene by the tetracysteine derived N4PyFe complex **2e** indicated that oxygen atoms were introduced into the ligand system. Under the applied conditions oxidation of the substrate could not be detected. Nevertheless, before **2e** can be ruled out as an active oxidation catalyst, it is suggested that optimised reaction conditions are first established.

5.8 Experimentals

General information

For general information about chemicals and instrumentation, see Chapter 3. N4PyFe (**2a**) was prepared as described previously.[2a,3,11a] For the preparation and analysis of ligand **2b**, see Chapter 4. For the preparation and analysis of ligands **1c–f** and iron(II) complexes **2e** and **2f**, see Chapter 3. GC analyses were performed on an Agilent 6890 Series GC System, equipped with a HP-1 methyl siloxane capillary column (30.0 m x 250 μm x 0.25 μm). The injection port and FID detector were set at 300°C. The temperature profile for the cyclohexene oxidation started at 50°C for 3 min, then was raised to 70°C at 3°C/min and maintained at that temperature for 8 min, followed by a temperature increase of 10°C/min to 100°C, and then to 250°C at 30°C/min. For the cyclohexane oxidation the initial temperature was set to 40°C for 15 min, followed by 10°C/min to 180°C and maintained at that temperature for 3 min. Calibration curves for the oxidation products shown in Scheme 5.4 have been determined using bromobenzene as internal standard.

[(N4Py4Br)Fe(MeCN)](ClO$_4$)$_2$ (2b)

To a suspension of N4Py4Br (93 mg, 0.14 mmol) in methanol (3 mL) was added Fe(ClO$_4$)$_2$·6 H$_2$O (56 mg, 0.15 mmol, 1.1 equiv) in acetonitrile (1.5 mL). The resulting clear dark red/brown solution was stirred at room temperature for 15 min. Slow diffusion of ethyl acetate into this solution furnished **2b** as red crystals (115 mg, 87%).

^{1}H NMR (CD$_3$CN, 300 MHz) δ 4.31 (dd, J_{AB} = 51.8, 18.5 Hz, 4H), 6.32 (s, 1H), 7.00 (d, J = 8.4 Hz, 2H), 7.75 (d, J = 8.4 Hz, 2H), 7.88 (dd, J = 8.4, 1.8 Hz, 2H), 8.10 (dd, J = 8.4, 1.8 Hz, 2H), 9.01 (d, J = 1.8 Hz, 2H), 9.10 (d, J = 1.8 Hz, 2H). ESI-MS [M−(ClO$_4$)$^-$−(MeCN)]$^+$ calcd for $C_{23}H_{17}Br_4ClFeN_5O_4$ *m/z* 833.7, found 833.6. [M−2(ClO$_4$)$^-$−(MeCN)]$^{2+}$ calcd for $C_{23}H_{17}Br_4FeN_5$ *m/z* 367.4, found 367.8. Anal. calcd for $C_{25}H_{20}Br_4Cl_2FeN_6O_8$ C 30.68; H 2.07; N 8.59. Found: C 30.48; H 2.27; N 8.36.

[(N4Py(CH$_2$OMe)$_4$)Fe(MeCN)](ClO$_4$)$_2$ (2c)

To a solution of **1c** (32 mg, 0.059 mmol) in acetonitrile (1.5 mL) was added Fe(ClO$_4$)$_2$·H$_2$O (17 mg, 0.066 mmol, 1.1 equiv). The deep red solution was placed in a sealed container and ethyl acetate was allowed to diffuse slowly into the solution. A dark red oil was formed after a week. The solution was removed and the oil dissolved in acetonitrile. A fine red powder was formed, which was isolated and redissolved in acetonitrile. Slow diffusion of ethyl acetate provided **2c** as red crystals after two weeks (9 mg, 18%).

^{1}H NMR (CDCl$_3$, 300 MHz) δ 3.29 (s, 6H), 3.34 (s, 6H), 4.32 (dd, J_{AB} = 27.9, 8.1 Hz, 4H), 4.38 (s, 4H), 4.47 (s, 4H), 6.31 (s, 1H), 7.04 (d, J = 8.1 Hz, 2H), 7.63 (d, J = 7.7 Hz, 2H), 7.85 (m, 4H), 8.82 (s, 2H), 8.92 (s, 2H). ESI-MS [M−(ClO$_4$)$^-$−(MeCN)]$^+$ calcd for C$_{31}$H$_{38}$ClFeN$_5$O$_8$ *m/z* 698.2, found 698.0. [M − 2(ClO$_4$)$^-$]$^{2+}$ calcd for C$_{33}$H$_{40}$FeN$_6$O$_4$ *m/z* 320.1, found 320.3. [M−2(ClO$_4$)$^-$−(MeCN)]$^{2+}$ calcd for C$_{31}$H$_{37}$FeN$_5$O$_4$ *m/z* 299.6, found 300.0.

[(N4Py(CH$_2$CH$_2$CH$_2$OMe)$_4$)Fe(MeCN)](ClO$_4$)$_2$ (2d)

To a solution of **1d** (35 mg, 0.054 mmol) in acetonitrile (1.5 mL) was added Fe(ClO$_4$)$_2$·6 H$_2$O (22 mg, 0.060 mmol, 1.1 equiv). The deep red solution was placed in a sealed container and ethyl acetate was allowed to slowly diffuse into the solution. A dark red oil was formed after a week. Repeated attempts failed to yield crystals and **2d** was obtained as a dark red/brown oil (41 mg, 84%).

^{1}H NMR (CDCl$_3$, 300 MHz) δ 1.85 (m, 8H), 2.80 (m, 8H), 3.25 (s, 6H), 3.32–3.48 (m, 8H), 3.39 (s, 6H), 4.36 (dd, J_{AB} = 31.7, 18.1 Hz, 4H), 6.32 (s, 1H), 7.07 (d, J = 8.1 Hz, 2H), 7.61 (d, J = 7.7 Hz, 2H), 7.86 (s, 4H), 8.83 (s, 2H), 8.94 (s, 2H). ESI-MS [M − (ClO$_4$)$^-$ − (MeCN)]$^+$ calcd for C$_{39}$H$_{53}$ClFeN$_5$O$_8$ *m/z* 810.3, found 810.3. [M−2(ClO$_4$)$^-$]$^{2+}$ calcd for C$_{41}$H$_{56}$FeN$_6$O$_4$ *m/z* 376.2, found 376.4. [M−2(ClO$_4$)$^-$−(MeCN)]$^{2+}$ calcd for C$_{39}$H$_{53}$FeN$_5$O$_4$ *m/z* 355.7, found 355.9.

Cyclic voltammetry of 2b

The cyclic voltammetry measurements were performed by dr. Scott Killeen at Unilever Research, Vlaardingen, The Netherlands, on a three-electrode electrochemical cell interfaced to a Princeton Applied Research potentiostat (Model 273A). The electrodes used (Working: 5 mm diameter glassy carbon, Counter: Pt wire, Reference: Ag/AgCl (3 M KCl)) were freshly cleaned by standard techniques prior to each measurement. The supporting electrolyte was 0.1 M tetrabutylammonium perchlorate (puriss, Fluka) in acetonitrile (analytical grade, Mallinckrodt Baker BV). The sample for analysis was prepared by dissolving **2b** (3 mg) in the electrolyte (10 mL). All measurements were carried out at 22°C and degassed with argon prior to measurement. For CV experiments the scan rate was 100 mV s^{-1} with an increment of 5 mV. The differential pulse voltammetry experiments were conducted at a scan rate of 10mV s^{-1} with an increment of 2 mV.

X-ray crystallography[29]

The selected crystal was mounted on a glass fibre and aligned on a *Bruker*[30] *SMART APEX CCD* diffractometer (Platform with full three-circle goniometer) equipped with a 4K *CCD* detector and a *Bruker KRYOFLEX* low-temperature device. Intensity measurements were performed using graphite monochromatic Mo–K$\overline{\alpha}$ radiation from a sealed ceramic diffraction

tube (50 kV/40 mA). All calculations for refinement and graphics were performed on a Pentium III (Debian-Linux) computer at the University of Groningen with the program packages *SHELXL*[31] (least-square refinements), a locally modified version of the program *PLUTO*[32] (preparation of illustrations) and the *PLATON*[33] package (checking the final results for missed symmetry with the *MISSYM* option, solvent accessible voids with the *SOLV* option, and calculation of geometric data).

Structure analysis of 2b. Crystallisation from acetonitrile/ethyl acetate initially afforded **2b** as red square platelets, with a monoclinic unit cell with a $P2_1/n$ space group, as well as a disordered and fractional occupation with the solvent molecules. Recrystallisation furnished red octahedral-shaped crystals. Dimensions of the crystal used for analysis: 0.40 x 0.32 x 0.22 mm.

The final unit cell was elucidated from the *xyz* centroids of 7444 reflections after refinement and integration using the programs *SMART* and *SAINT*. In total 1800 frames were collected with an exposure time of 10 s per frame. Intensity data was corrected for Lorentz and polarisation effects, as well as for decay and absorption: a semi-empirical absorption correction was applied, based on the intensities of symmetry-related reflections measured at different angular settings (*SADABS*),[34] and reduced to F_o^2. The program suite *SHELXTL* was used for space group determination (*XPREP*).[31] The structure was solved by automated Patterson methods using the program *DIRDIF*.[35] The positional and (an)isotropic displacement parameters for the non-hydrogen atoms were refined on F^2 using full-matrix least-squares procedures.

The asymmetric unit cell contains eleven moieties: two iron complexes (cations) and four perchlorate anions, one ethyl acetate and four acetonitrile solvent molecules with no atom setting at a special position. The triclinic unit cell contains twenty-two discrete units separated by normal van der Waals distances.

Crystal data. $([C_{25}H_{20}Br_4FeN_6]^{2+})_2.(ClO_4^-)_4.C_4H_8O_2.(C_2H_3N)_4$; M = 2209.9 gmol^{-1}; triclinic; space group $P\bar{1}$ with a = 16.8760(8), b = 16.9697(8), c = 17.1403(8) Å; α = 64.758(1)°, β = 63.885(1)°, γ = 77.286(1)°; V = 3983.5(3) Å^3; Z = 2; D_x = 1.842 gcm^{-3}; λ = 0.71073 Å; μ = 45.86 cm^{-1}; F(000) = 2176; T = 90 K; *GooF* = 1.030; $wR(F^2)$ = 0.1105 for 20152 reflections and 974 parameters; $R(F)$ = 0.0423 for 15627 reflections obeying the $F_o \geq 4.0\ \sigma(F_o)$ criterion of observability.

Structure analysis of 2c. Red coloured triangular/block-shaped crystals were obtained after a troublesome crystallisation from acetonitrile by slow diffusion of ethyl acetate. Most of the crystals were joined together, which hampered the X-ray structure determination, however a small suitable specimen was found. Dimensions of the crystal used for analysis: 0.10 x 0.10 x 0.10 mm.

The final unit cell was obtained from the *xyz* centroids of 6038 reflections after refinement and integration using the programs *SMART* and *SAINT*. A total of 1800 frames were collected with an exposure time of 30 s per frame. Intensity data was corrected for Lorentz and polarisation effects, scale variation, and for decay and absorption. A multi-scan absorption correction was applied, based on the intensities of symmetry-related reflections measured at different angular settings (*SADABS*),[34] and reduced to F_o^2. The program suite *SHELXTL* was used for space group determination (*XPREP*).[31] The *E*-statistics of the triclinic unit cell were indicative of a centrosymmetric space group. The structure was solved by direct methods using

SIR-97.[36] The positional and anisotropic displacement parameters for the non-hydrogen atoms were refined. Refinement was complicated by a disorder problem: from the solution it was clear that one of the two perchlorate anions was highly disordered. The electron density of the atoms appeared to be diffuse, indicating transformational disorder. A disorder model with bond restraints and two different orientations were also introduced into the subsequent refinement. The site-occupation factor of the major fraction of the disordered perchlorate anions was refined to a value of 0.519(5).

The asymmetric unit consists of four moieties: a cationic iron complex, two perchlorate anions, one of which is highly disordered, and one acetonitrile solvent molecule. Reduced cell calculations did not indicate any higher metric lattice symmetry and examination of the final atomic co-ordinates of the structure did not yield any additional metric symmetry elements.
Crystal data. $[C_{33}H_{40}FeN_6O_4]^{2+}.(ClO_4^-)_2.C_2H_3N$; M_r = 880.52 gmol^{-1}; triclinic; space group *P*−1 with *a* = 10.2381(6), *b* = 13.1842(7), *c* = 16.4591(9) Å; α = 67.046(1)°, β = 77.949(1)°, γ = 75.701(1)°; *V* = 1966.57(19) Å^3; *Z* = 2; D_x = 1.487 gcm^{-3}; λ = 0.71073 Å; μ = 5.90 cm^{-1}; *F*(000) = 916; T = 100 K; *GooF* = 1.028; *wR*(F^2) = 0.1485 for 8855 reflections and 567 parameters, 8 restraints; *R*(*F*) = 0.0584 for 6275 reflections obeying the $F_o \geq 4.0\ \sigma(F_o)$ criterion of observability.

Catalytic oxidation of cyclohexene and cyclohexane

A 3.50 mM stock solution of the catalyst was prepared in acetonitrile. For the experiment a 1.0 mL aliquot was transferred into the reaction flask and the solvent evaporated *in vacuo*. A stock solution of the substrate (43.75 mmol) and bromobenzene (4.37 mmol) as an internal standard was prepared in the appropriate solvent (50.00 mL). A 4.0 mL aliquot of stock solution was added to the catalyst under a nitrogen atmosphere. Samples were taken at designated intervals, filtered over a small amount of silica gel, washed with diethyl ether/methanol (9:1, 1 mL), and analysed by gas chromatography. Duplicate experiments were performed to calculate the average number of turnovers (margin of error ~1 turnover).
Procedure A: The oxidation was initiated by injection of H_2O_2 (35 µL, 10 M, 30% in water) to the reaction mixture (catalyst/H_2O_2/substrate = 1:100:1000) at 20°C. Samples (200 µL) were taken at intervals of 5, 10, 20, 30, 45, and 60 min.
Procedure B: The H_2O_2 (0.75 mL, 10 M, 30% in water) was administered to the reaction mixture (catalyst/H_2O_2/substrate = 1:2000:1000) by a syringe pump over 1 h at 20°C. Samples (200 µL) were taken at intervals of 30, 60, and 90 min.

ABTS oxidation

All ABTS oxidation experiments were performed in 0.1 M acetate buffers at pH 3.0, 3.5, 4.0, and 4.5 using a magnetically stirred, thermostatically controlled quartz cuvette at 20°C. The increase in absorption due to the $ABTS^{+\bullet}$ radical cation formation was monitored by a UV-Vis spectrophotometer at 660 nm (ε 1.47 x 10^4 M^{-1}cm^{-1})[15b] at intervals of 1 s for 400 s with an incremental cycle time of 10% after an initial time of 60 s. The experimental conditions were identical to those described previously by Dr. C. T. Choma.[24]

5.9 References and notes

1. For an explanation of the abbreviations used, see Appendix 1 (p. 149).
2. (a) Roelfes, G.; Lubben, M.; Chen, K.; Ho, R. Y. N.; Meetsma, A.; Genseberger, S.; Hermant, R. M.; Hage, R.; Mandal, S. K.; Young, V. G., Jr.; Zang, Y.; Kooijman, H.; Spek, A. L.; Que, L., Jr.; Feringa, B. L. *Inorg. Chem.* **1999**, *38*, 1929–1936. (b) Roelfes, J. G., In *Models for Non-Heme Iron Containing Oxidation Enzymes*, Ph. D. thesis, Groningen, 2000.
3. (a) Lubben, M., In *Model Systems for Iron and Copper Containing Oxygenases*, Ph. D. thesis, Groningen, 1994; pp. 43–71. (b) Lubben, M.; Meetsma, A.; Wilkinson, E. C.; Que, L., Jr.; Feringa, B. L. *Angew. Chem. Int. Ed. Engl.* **1995**, *34*, 1512–1514.
4. See Appendix 2 (p. 151) for the structures and one-letter abbreviations of the amino acids.
5. See Chapter 3 for the characterisation of **2e** and **2f**.
6. Selected bond distances originate from residue 2 in the unit cell of **2b**. For residue 1 the bond lengths are: Fe–N1, 1.966(3); Fe–N2, 1.967(4); Fe–N3, 1.957(3); Fe–N4, 1.952(3); Fe–N5, 1.970(4); Fe–N6, 1.929(4); Fe–$N_{py-mean\ plane}$, 0.200(1).
7. Solomon, E. I.; Brunold, T. C.; Davis, M. I.; Kemsley, J. N.; Lee, S.-K.; Lehnert, N.; Neese, F.; Skulan, A. J.; Yang, Y.-S.; Zhou, J. *Chem. Rev.* **2000**, *100*, 235–349.
8. The iron(II) complex of the N4Py derivative **6b** in Chapter 2 (p. 34).
9. C. T. Choma, *personal communication*.
10. Ho, R. Y. N.; Roelfes, G.; Hermant, R.; Hage, R.; Feringa, B. L.; Que, L., Jr. *Chem. Commun.* **1999**, 2161–2162.
11. (a) Roelfes, G.; Lubben, M.; Leppard, S. W.; Schudde, E. P.; Hermant, R. M.; Hage, R.; Wilkinson, E. C.; Que, L., Jr.; Feringa, B. L. *J. Mol. Catal. A: Chem.* **1997**, *117*, 223–227. (b) Roelfes, G.; Lubben, M.; Hage, R.; Que, L., Jr.; Feringa, B. L. *Chem. Eur. J.* **2000**, *6*, 2152–2159.
12. Arends, I. W. C. E.; Ingold, K. U.; Wayner, D. D. M. *J. Am. Chem. Soc.* **1995**, *117*, 4710–4711.
13. (a) Everse, J., Everse, K. E., Grisham, M. B., In *Peroxidases in Chemistry and Biology*; CRC Press: Boca Raton, USA, 1991; Vol. 2, pp. 1–24. (b) Ball, D. P., In *Essays in Biochemistry*, *Metalloproteins*; Portland Press: UK, 1999; Vol. 34, pp. 51–69.
14. (a) Cunningham, I. D.; Bachelor, J. L.; Pratt, J. M. *J. Chem. Soc.*, *Perkin Trans. 2* **1991**, 1839–1843. (b) Chuang, W.-J.; Chang, Y.-D.; Jeng, W.-Y. *J. Inorg. Biochem.* **1999**, *75*, 93–97.
15. (a) Casella, L.; Poli, S.; Gullotti, M.; Selvaggini, C.; Beringhelli, T.; Marchesini, A. *Biochemistry* **1994**, *33*, 6377–6386. (b) Casella, L.; De Gioia, L.; Silvestri, G. F.; Monzani, E.; Redaelli, C.; Roncone, R.; Santagostini, L. *J. Inorg. Biochem.* **2000**, *79*, 31–40.
16. (a) Adams, P. A.; Goold, R. D. *J. Chem. Soc.*, *Chem. Commun.* **1990**, 97–98. (b) Adams, P. A. *J. Chem. Soc.*, *Perkin Trans. 2* **1990**, 1407–1414.
17. (a) Maehly, A. C.; Chance, B., In *Methods in Biochemical Analysis*; Glick, D., Ed.; 1954; Vol. 1, pp. 385–387. (b) Chance, B.; Maehly, A. C., In *Methods in Enzymology*; Colowick, S. P.; Kaplan, N. O., Eds.; Academic Press: New York, USA, 1964; pp. 770–773.
18. Iffland, A.; Tafelmeyer, P.; Gendreizig, S.; Johnsson, K. *Chimia* **2001**, *55*, 291–294.

19. (a) Fujita, A.; Senzu, H.; Kunitake, T.; Hamachi, I. *Chem. Lett.* **1994**, 1219–1222. (b) Doerge, D. R.; Divi, R. L.; Churchwell, M. I. *Anal. Biochem.* **1997**, *250*, 10–17. (c) Ochoe de Aspuru, E.; Zatón, A. M. L. *Spectrochim. Acta A* **1999**, *55*, 2343–2346. (d) Sakamoto, S.; Obataya, I.; Ueno, A.; Mihara, H. *J. Chem. Soc.*, *Perkin Trans. 2* **1999**, 2059–2069. (e) Obataya, I.; Kotaki, T.; Sakamoto, S.; Ueno, A.; Mihara, H. *Bioorg. Med. Chem. Lett.* **2000**, *10*, 2719–2722.
20. Other structures have also been suggested for tetraguaiacol. See references 17a and 19b.
21. (a) Childs, R. E.; Bradsley, W. G. *Biochem. J.* **1975**, *145*, 93–103. (b) Moffet, D. A.; Certain, L. K.; Smith, A. J.; Kessel, A. J.; Beckwith, K. A.; Hecht, M. H. *J. Am. Chem. Soc.* **2000**, *122*, 7612–7613.
22. Poigny, S.; Guyot, M.; Samadi, M. *Tetrahedron* **1998**, *54*, 14791–14802.
23. (a) Kersten, P. J.; Tien, M.; Kalyanaraman, B.; Kirk, T. K. *J. Biol. Chem.* **1985**, *260*, 2609–2612. (b) Kersten, P. J.; Kalyanaraman, B.; Hammel, K. E.; Reinhammar, B.; Kirk, T. K. *Biochem. J.* **1990**, *268*, 475–480. (c) Schoemaker, H. E. *Recl. Trav. Chim. Pays-Bas* **1990**, *109*, 255–272. (d) Popp, J. L.; Kirk, T. K. *Arch. Biochem. Biophys.* **1991**, *288*, 145–148.
24. Choma, C. T.; Schudde, E. P.; Kellogg, R. M.; Robillard, G. T.; Feringa, B. L. *J. Chem. Soc.*, *Perkin Trans. 1* **1998**, 769–773.
25. Florence, T. M. *J. Inorg. Biochem.* **1985**, *23*, 131–141.
26. Wolfenden, B. S.; Willson, R. L. *J. Chem. Soc.*, *Perkin Trans. 2* **1982**, 805–812.
27. Rush, J. D.; Koppenol, W. H. *J. Am. Chem. Soc.* **1988**, *110*, 4957–63.
28. De Nooy, A. E. J.; Besemer, A. C.; Van Bekkum, H. *Synthesis* **1996**, 1153–1174.
29. Data collection, structure analysis and refinement was carried out by A. Meetsma, Crystal Structure Center, Chemical Physics, Materials Science Center, University of Groningen: The Netherlands.
30. *SMART*, *SAINT*, *SADABS*, *XPREP* and *SHELXTL/NT*, Smart Apex *Software Reference Manuals*, Bruker AXS, Inc.: Madison, Wisconsin, USA, 2000.
31. Sheldrick, G. M., *SHELXL-97*, *Program for the Refinement of Crystal Structures*, University of Göttingen: Germany, 1997.
32. Meetsma, A., *PLUTO. Molecular Graphics Program*, University of Groningen: The Netherlands, 2001.
33. Spek, A. L., *PLATON. Program for the Automated Analysis of Molecular Geometry* (*A Multipurpose Crystallographic Tool*), University of Utrecht: The Netherlands, February 2002.
34. Sheldrick, G. M., *SADABS* (Version 2), *Empirical Absorption Correction Program*, University of Göttingen: Germany, 2000.
35. Beurskens, P. T.; Beurskens, G.; De Gelder, R.; García-Granda, S.; Gould, R. O.; Israël, R.; Smits, J. M. M., *The DIRDIF-99 program system*, Crystallography Laboratory, University of Nijmegen: The Netherlands, 1999.
36. Altomare, A.; Burla, M. C.; Camalli, M.; Cascarano, G. L.; Giacovazzo, C.; Guagliardi, A.; Moliterni, A. G. G.; Polidori, G.; Spagna, R. *J. Appl. Cryst.* **1999**, *32*, 115–119.